



science.sciencemag.org/content/364/6440/552/suppl/DC1

## Supplementary Materials for

### **Structures of the M1 and M2 muscarinic acetylcholine receptor/ G-protein complexes**

Shoji Maeda\*, Qianhui Qu\*, Michael J. Robertson, Georgios Skiniotis†,  
Brian K. Kobilka†

\*These authors contributed equally to this work.

†Corresponding author. Email: [yiorgo@stanford.edu](mailto:yiorgo@stanford.edu) (G.S.); [kobilka@stanford.edu](mailto:kobilka@stanford.edu)  
(B.K.K.)

Published 10 May 2019, *Science* **364**, 552 (2019)

DOI: 10.1126/science.aaw5188

#### **This PDF file includes:**

Materials and Methods

Figs. S1 to S16

Tables S1 to S3

References

## Materials and methods

### Protein expression and purification

Wild type human M1R was modified to contain N-terminal FLAG-tag and C-terminal histidine-tag. N2Q and N12Q mutations were introduced to remove glycosylation sites. The construct contains an unintentional mutation N110Q; however, this mutation has no significant effect in the receptor function(7). Residues 233-344 of ICL3 were removed. The M1R gene was cloned into pFastBac1 vector and expressed in Sf9 insect cells using baculovirus infection system. Human M2R gene containing N-terminal FLAG-tag and C-terminal EGFP-histidine-tag following to the HRV-3C cleavage site was also cloned into pFastBac1 vector. Residues 233-359 of ICL3 were removed in M2R. Cells were solubilized in 1% DDM, 0.2% CHS in the presence of 10uM atropine and 0.05%LMNG, and the soluble fraction was purified by Ni-chelating sepharose chromatography. The eluted protein was supplemented with 2mM CaCl<sub>2</sub>, loaded onto M1 anti-FLAG immunoaffinity column and detergent exchanged to 0.01%MNG with the buffer containing an agonist iperoxo. Receptor was eluted in a buffer consisting of 100mM NaCl, 20mM Hepes pH 7.5, 0.01% LMNG, 0.001% CHS with 10uM iperoxo, and further purified by SEC on a superdex 200 10/300 column in a buffer containing 10uM iperoxo. Monomeric fractions were pooled and flash frozen for the complex formation. Receptor mutants were generated using PCR-based mutagenesis with the wild type receptors as template and all the mutations were confirmed by DNA sequencing. A schematic diagram of the receptor constructs used in this study is provided (Fig S16).

Heterotrimeric G-proteins were expressed and purified as follows: For the expression of G<sub>oA</sub> protein series, *Trichoplusia ni* (Hi5) insect cells were coinfecting with viruses encoding the wild type G $\alpha_{oA}$  or G $\alpha_{oAiN}$ , and the wild-type human G $\beta_1\gamma_2$  subunits. G $\alpha_{oAiN}$  was made by introducing mutations of E9D, R10K, L13V, and A13M. For the expression of G<sub>11</sub> protein series, three viruses were coinfecting encoding the wild-type human G $\alpha_{11}$  or G $\alpha_{11iN}$  chimera(19), the wild-type human G $\beta_1\gamma_2$  subunits, and Ric8A. We provide a schematic figure of the design of the chimeric G-proteins for clarity (Fig. S1). In order to facilitate the purification, His-tag with HRV-3C protease cleavable site is attached at the amino terminus of the G $\beta_1$  subunit. Cells were harvested 48 hours post infection, lysed in hypotonic buffer and lipid-modified heterotrimeric G-protein was extracted in a buffer

containing 1% sodium cholate and 0.05% DDM. The soluble fraction was purified using Ni-chelating sepharose chromatography, and the detergent was exchanged from cholate/DDM mixture to DDM alone. After elution, lambda protein phosphatase, calf intestine phosphatase, Antarctic phosphatase, and HRV-3C protease was added and the protein was dialyzed against a buffer consisting of 20mM Hepes pH 7.5, 100mM NaCl, 1mM MgCl<sub>2</sub>, 1mM MnCl<sub>2</sub>, 0.05% DDM, 100μM TCEP, 10μM GDP. Cleaved heterotrimeric G-protein was further purified by reloading over Ni-sepharose resin. For the functional assay, the protein was further purified by ion-exchange chromatography using a MonoQ 10/100 column to remove excess Gβ<sub>1</sub>γ<sub>2</sub> subunits.

ScFv16 were expressed from *Trichoplusia ni* Hi5 insect cells as a secreted protein using the baculovirus infection system. The media was harvested 96h post infection and the protein was purified by Ni-sepharose chromatography as described previously. Briefly, the media from baculovirus infected cells was pH balanced by addition of 50mM Tris pH 7.5 and chelating agents were quenched by addition of 1 mM nickel chloride and 5 mM calcium chloride and incubation for 1 hr at 25 °C with constant stirring. Resulting precipitates were removed by centrifugation and the supernatant was loaded over Ni-sepharose chromatography column. The column was washed with a high salt buffer (20 mM Hepes pH 7.5, 500 mM NaCl, and 20 mM imidazole) followed by a low salt buffer (20 mM Hepes pH 7.5, 100 mM NaCl, and 20 mM imidazole). The protein was eluted with the elution buffer (20 mM Hepes pH 7.5, 100 mM NaCl, and 250 mM imidazole) and the carboxy-terminal his-tag was cleaved by incubation with HRV-3C protease during dialysis against a buffer consisting of 20 mM Hepes pH 7.5 and 100 mM NaCl. Cleaved protein was further purified by reloading over Ni-NTA resin. The flow through was collected and purified over a size exclusion chromatography using a Hiloal superdex 200 16/600 pg column. ScFv16 peak fractions were pooled, concentrated, and flash frozen in liquid nitrogen until use.

### **Complex formation of M1R-G<sub>11iN</sub>-scFv16 and M2R-G<sub>0AiN</sub>-scFv16**

The M1R-G<sub>11iN</sub>-scFv16 and M2R-G<sub>0AiN</sub>-scFv16 complexes were formed essentially in the same way as described previously(10, 19). Briefly, purified receptors and excess molar ratio of G-protein were mixed together in the buffer consisting of 20mM Hepes pH7.5, 100mM NaCl, 1% LMNG, 100μM TCEP, 200uM iperoxo. In the case of M2R,

purified HRV-3C protease (in-house prepared) was included to cleave off the C-terminal EGFP. The protein was incubated at room temperature for 1h then added with apyrase to enzymatically remove GDP from G-protein. The protein was further incubated for at least 3h on ice, diluted with 10 fold more volume of the buffer consisting of 20mM Hepes pH7.5, 100mM NaCl, 0.01% LMNG, 0.03%GDN, 10uM iperoxo, then loaded over FLAG immunoaffinity column. The detergent concentration was lowered during the wash to the mixture of 0.00075% LMNG and 0.00025% GDN. The complex was eluted with the elution buffer followed by incubation with purified scFv16 for 2h on ice. The scFv16-bound complex was further purified by a size exclusion chromatography on a superdex 200 Increase 10/300 column to remove uncoupled receptor and excess scFv16. The monomeric complex peak was collected, supplemented with 400uM iperoxo and 400uM VU0357017 for M1R-G<sub>11iN</sub>-scFv16 or 400uM LY2119620 for M2R-G<sub>oAiN</sub>-scFv16, and concentrated over 30mg/ml for making the cryo grid.

### **Cryo-EM sample preparation and image acquisition**

The homogeneity of purified M1R-G<sub>11iN</sub>-scFv16 complex was evaluated by negative stain EM(57). For cryo-EM, 3.5  $\mu$ L sample was directly applied to glow-discharged 200 mesh gold grids (Quantifoil R1.2/1.3) and vitrified using a FEI Vitrobot Mark IV (Thermo Fisher Scientific). Image were collected on a Titan Krios (SLAC/Stanford) operated at 300 keV at a nominal magnification of 130,000X using a Gatan K2 Summit direct electron detector in counted mode, corresponding to a pixel size of 1.06Å (Supplementary Figures 2,3). Movie stacks were obtained with a defocus range of -1.0 to -2.0  $\mu$ m, using SerialEM(58) with a set of customized scripts enabling automated low-dose image acquisition. Each movie stack was recorded for a total of 8 seconds with 0.2s exposure per frame and exposure dose set to 7 electrons per pixel per second. The M2R-G<sub>oAiN</sub>-scFv16 complex was purified and imaged with the same parameters as the M1R-G<sub>11iN</sub>-scFv16 sample. The only difference in the case of M2R-G<sub>oAiN</sub>-scFv16 is that data were collected both in the absence or presence of  $\beta$ -OG, which was added right before grid preparation in an effort to rescue more complex from damage during cryo-EM specimen preparation. We note that the addition of  $\beta$ -OG resulted in a modest increase in intact M2R-G<sub>oAiN</sub>-scFv16 complexes from 3%~6% to 7.5%-11% of all autopicked particles.

### **Cryo-EM data processing**

For M1R-G<sub>11iN</sub>-scFv16 complex, a total 5090 image stacks were collected and subjected to beam-induced motion correction using MotionCor2(59). Contrast transfer function parameters for each micrograph were estimated from the exposure-weighted averages of all frames by Gctf v1.06(60), implemented in RELION2.1(61). Particles were autopicked, extracted with a box size of 220 pixels, and subjected to 2D classification, 3D classification and initial refinement using RELION2.1 (Supplementary Figure 2). The cryo-EM map of  $\mu$ OR-G<sub>i</sub>-scFv16 complex(15) was low-pass filtered to 60Å and used as initial reference model for 3D classification. A dataset of 277,988 particles were subjected to 3D auto-refinement, resulting in an initial 3.5Å density map. Further Bayesian polishing of these particle projections was performed in RELION3.0, followed by another round of auto-refinement, which generated a final 3.3Å map determined by gold standard Fourier shell correlation using the 0.143 criterion. Local resolution estimation was performed with the Bsoft package(62) using the two unfiltered half maps .

For the M2R-G<sub>oAiN</sub>-scFv16 complex, a total of five datasets (>20,000 images) were collected (three datasets without  $\beta$ -OG and two with  $\beta$ -OG; Supplementary Figure 3). Each dataset was individually subjected to motion correction, CTF estimation, autopicking, 2D classification and 3D classification in RELION2.1. After 3D classification, the stable classes with well-defined density features were combined into two separate subsets, with or without  $\beta$ -OG. The two subsets (249,929 particles without  $\beta$ -OG and 278,258 particles with  $\beta$ -OG) were both auto-refined to the same reported 4.5Å resolution. The two subsets were subsequently merged and subjected to another round of 3D classification, thereby isolating a final partition of 261,730 particles. Auto-refinement on this particle set resulted in a 4.0Å map. Further Bayesian polishing applied to these particles in RELION3.0 improved the density map with an indicated nominal resolution of 3.6Å. Local resolution estimation was also performed with the Bsoft package.

### **Model building and refinement**

Homology models of active-state M1R, M2R, G<sub>11i</sub>, and G<sub>oA</sub> were built by SWISS-MODEL(63) using active M2R (PDB code 4MQS) for the receptor and  $\beta$ 2AR/G<sub>s</sub> (PDB code 3sn6) for the G-protein as template models, respectively. All models were docked into the EM density map using Chimera(64) followed by iterative manual adjustment in COOT(65) and phenix.real\_space\_refine in Phenix(66). The model statistics was

validated using Molprobit(67). Structural figures were prepared by Chimera(64), ChimeraX(68) or PyMOL (<https://pymol.org/2/>). The final refinement statistics were provided in Supplementary Table 3. The extent of any model overfitting during refinement was measured by refining the final model against one of the half-maps and by comparing the resulting map versus model FSC curves with the two half-maps and the final model.

### **Docking simulations of iperoxo**

M1R was prepared for docking by addition of missing sidechain atoms and hydrogen bonding optimization with Schrödinger's Maestro protein preparation (**Schrödinger Release 2018-4**: Maestro, Schrödinger, LLC, New York, NY, 2018). Glide extra precision (XP) docking(69) was executed on the prepared structure with iperoxo. The top five unique poses were subjected to real space refinement in phenix(66) before being subjected to Glide scoring in place.

### **Radioligand binding assay**

Cell membranes were prepared from Sf9 cells expressing each receptor construct. [<sup>3</sup>H]NMS affinity of M1R constructs were determined by saturation binding assays by incubating the membrane with varying concentrations of [<sup>3</sup>H]NMS for 2h at room temperature in a buffer consisting of 20mM HEPES pH7.5, 100mM NaCl, 5mM MgCl<sub>2</sub> and 0.1%BSA. Radioligand competition binding assays were carried out by incubating the membrane with a fixed concentration of [<sup>3</sup>H]NMS and varying concentrations of iperoxo for 2h at room temperature. G<sub>11</sub> titration competition binding assay was carried out by incubating the membrane with a fixed concentration of [<sup>3</sup>H]NMS and 2 μM iperoxo with varying concentration of purified G<sub>11</sub> for 2h. Non-specific binding was measured in the presence of 10μM atropine, and reactions were harvested by a rapid filtration through GF/B filters. Data were analyzed using Prism7.

### **GTP turnover assay**

GTP turnover was analysed using a modified protocol of the GTPase-Glo™ assay (Promega). The reaction was started by mixing purified receptor bound with iperoxo and G protein in an assay buffer containing 20 mM HEPES, pH 7.5, 100 mM NaCl, 0.01% LMNG, 100 μM TCEP, 10 mM MgCl<sub>2</sub>, 100 μM iperoxo, 10 μM GDP and 5 μM GTP.

For the assays using G<sub>11</sub>, GDP was omitted from the reaction buffer. After incubation for 120 min, reconstituted GTPase-Glo™ reagent was added to the sample and incubated for 30 min at room temperature. Luminescence was measured following the addition of the detection reagent and incubation for 10 min at room temperature using a SpectraMax Paradigm plate reader. The relative light unit (RLU) was corrected by the values of G-protein alone and normalized to the response in the presence of the WT receptor.

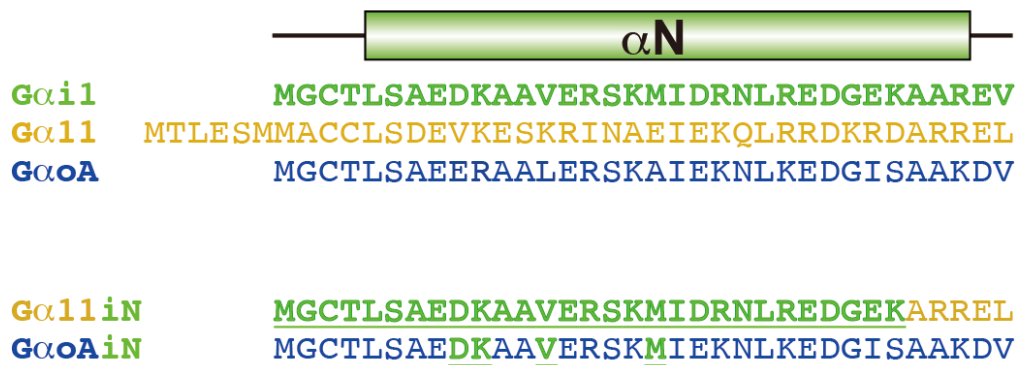


**Fig. S1. Schematic representation of G-protein chimera/mutant constructs used in this study.** Upper panel: Sequences of the N-terminal region of each wild-type G-protein  $\alpha$ -subunit with the secondary structure representation. Lower panel: Sequences of the chimeric G-protein  $\alpha$ -subunits. Amino acid residues derived from G $\alpha$ i1 are colored in green.



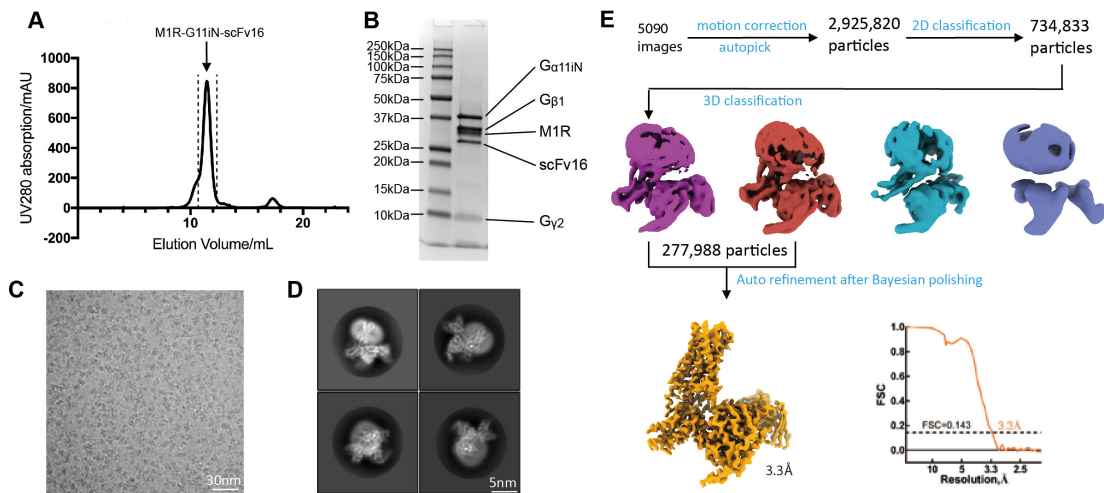


**Fig. S2. M1R-G<sub>11iN</sub>-scFv16 preparation and cryo-EM data processing.** **A.** Representative elution profile of purified M1R-G<sub>11iN</sub>-scFv16 complex on Superdex200Increase 10/300 size-exclusion column. **B.** SDS-PAGE analysis of purified M1R-G<sub>11iN</sub>-scFv16 complex. **C.** Representative cryo-EM image of M1R-G<sub>11iN</sub>-scFv16 complex. Scale bar 30nm. **D.** Representative 2D averages showing distinct structural features from different views. Scale bar, 5nm. **E.** Work-flow of cryo-EM data processing. The final 3.3 Å resolution map is colored in orange at the bottom left. ‘Gold standard’ FSC curve indicates overall nominal resolution at 3.3 Å using the FSC = 0.143 criterion.

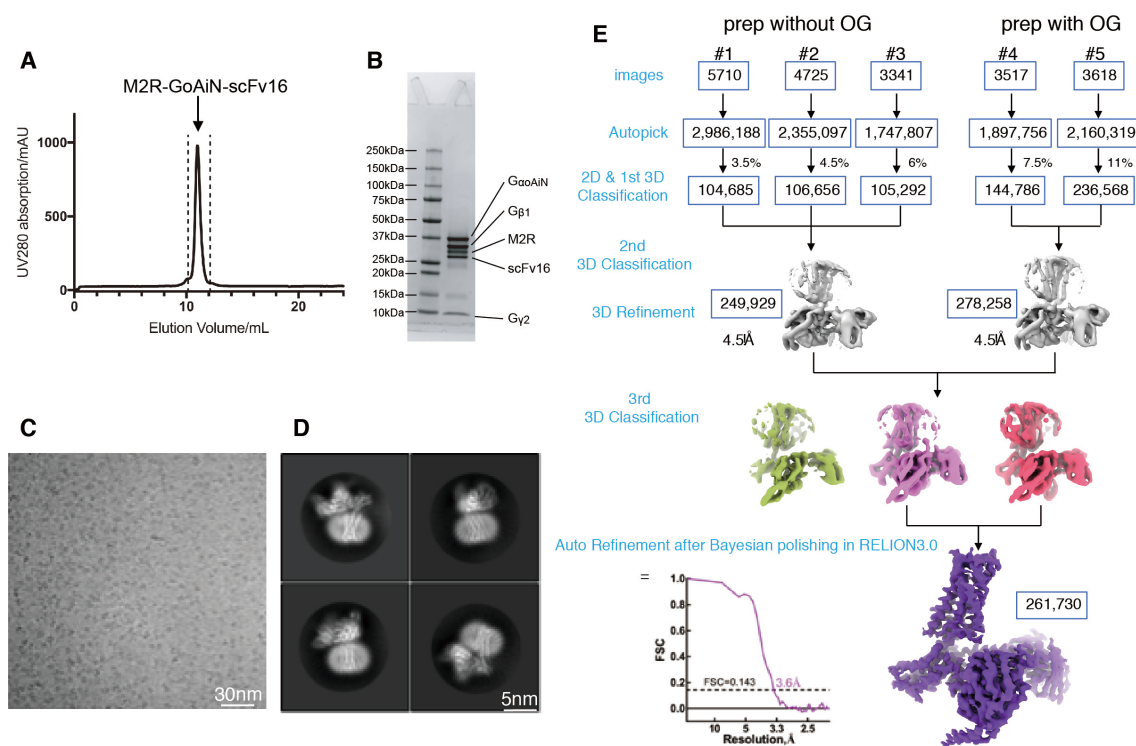


**Fig. S3. M2R-G<sub>0</sub>AiN-scFv16 preparation and cryo-EM data processing.** **A.** Representative elution profile of purified M2R-G<sub>0</sub>AiN-scFv16 complex on Superdex200Increase 10/300 size-exclusion column. **B.** SDS-PAGE analysis of purified M2R-G<sub>0</sub>AiN-scFv16 complex. **C.** Representative cryo-EM image of M2R-G<sub>0</sub>AiN-scFv16 complex. Scale bar, 30nm. **D.** Representative 2D averages showing distinct structural features from different views. Scale bar, 5nm. **E.** Work-flow of cryo-EM data processing of M2R-G<sub>0</sub>AiN-scFv16. The final 3.6 Å resolution map is colored in purple at the bottom right. ‘Gold standard’ FSC curve indicates overall nominal resolution at 3.6 Å using the FSC = 0.143 criterion.

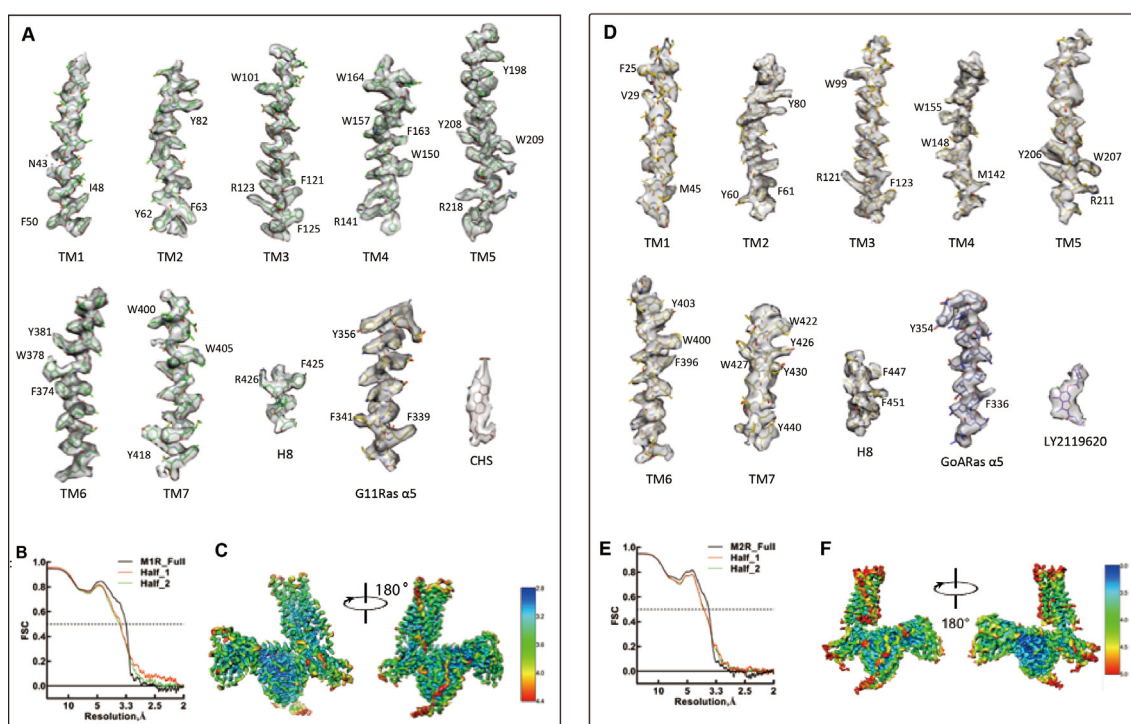


**Fig. S4. Cryo-EM map and refined structure.** **A.** Cryo-EM density map and the model of M1R-G<sub>11iN</sub>-scFv16 are shown for all transmembrane helices and helix 8 of M1R as well as  $\alpha 5$  helix of G $\alpha_{11iN}$  and CHS. **B.** Cross-validation of model to cryo-EM density map for M1R-G<sub>11iN</sub>-scFv16. The model was refined against one half map, and FSC curves were calculated between this model and the final cryo-EM map (full dataset, black) of the outcome of model refinement with a half map versus the same map (red), and of the outcome of model refinement with a half map versus the other half map (green). **C.** Local resolution map of M1R-G<sub>11iN</sub>-scFv16 complex. **D.** Cryo-EM density map and the model of M2R-G<sub>0AiN</sub>-scFv16 are shown for all transmembrane helices and helix 8 of M2R as well as  $\alpha 5$  helix of G $\alpha_{0AiN}$  and LY2119620. **E.** Cross-validation of model to cryo-EM density map for M2R-G<sub>0AiN</sub>-scFv16. The model was refined against one half map, and FSC curves were calculated between this model and the final cryo-EM map (full dataset, black) of the outcome of model refinement with a half map versus the same map (red), and of the outcome of model refinement with a half map versus the other half map (green). **F.** Local resolution map of M2R-G<sub>0AiN</sub>-scFv16.

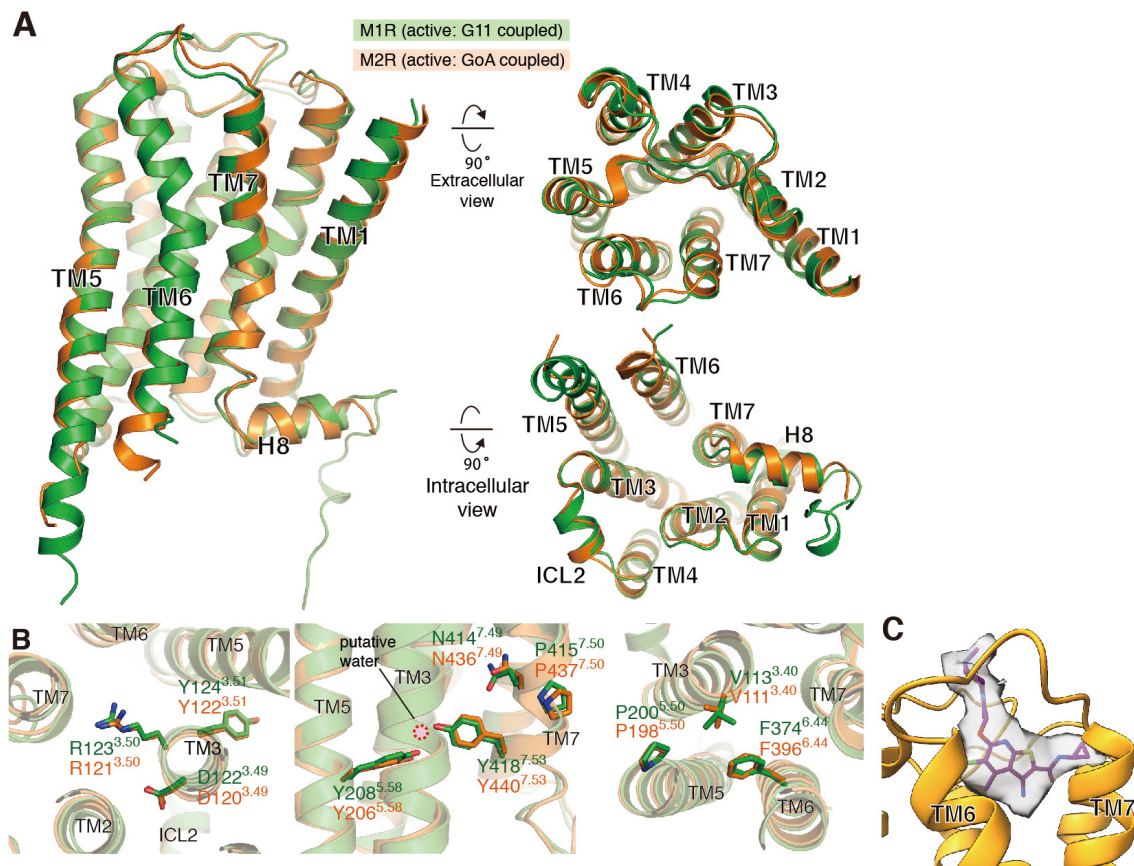


**Fig. S5. Comparison of active muscarinic structures.** **A.** Superimposition of active M1R and active M2R viewed from parallel to (left) and perpendicular to the membrane (right). Active M1R is colored in green and active M2R in orange. **B.** Similarity of important structural motifs for the activation: DRY (left), NPxxY (middle), and PI(V)F (right) motif. A putative water molecule coordinated by the conserved tyrosines found in the structure of MOR/Nb39 (PDB ID: 5C1M) is shown as a dashed circle in the NPxxY panel. Each residue number and Ballesteros-Weinstein number is provided. **C.** Map and model of the allosteric modulator LY2119620. LY2119620 is shown as sticks in purple.

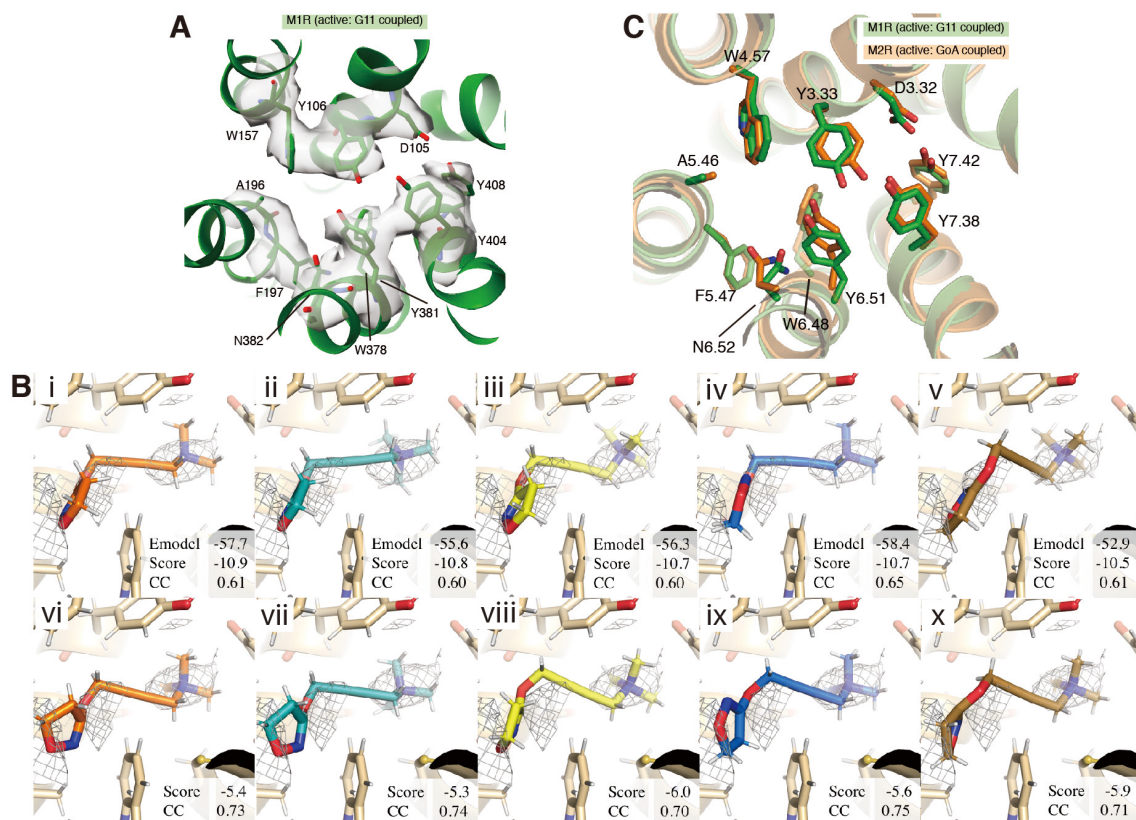


**Fig. S6. Iperoxo binding mode in M1R and M2R.** **A.** Map of the residues forming the iperoxo binding pocket in M1R. **B.** Comparison of poses for iperoxo bound to M1R. CC is the real space cross correlation of the pose to the cryo-EM map. **i-v.** The top five docked poses from Schrödinger's Glide, where Emodel and Score are the Emodel and XP Glide score values. **vi-x.** The same poses after real space refinement to the density, where score is the Glide score calculated in place. **C.** Superposition of the side-chain organization forming iperoxo binding pocket between M1R and M2R.

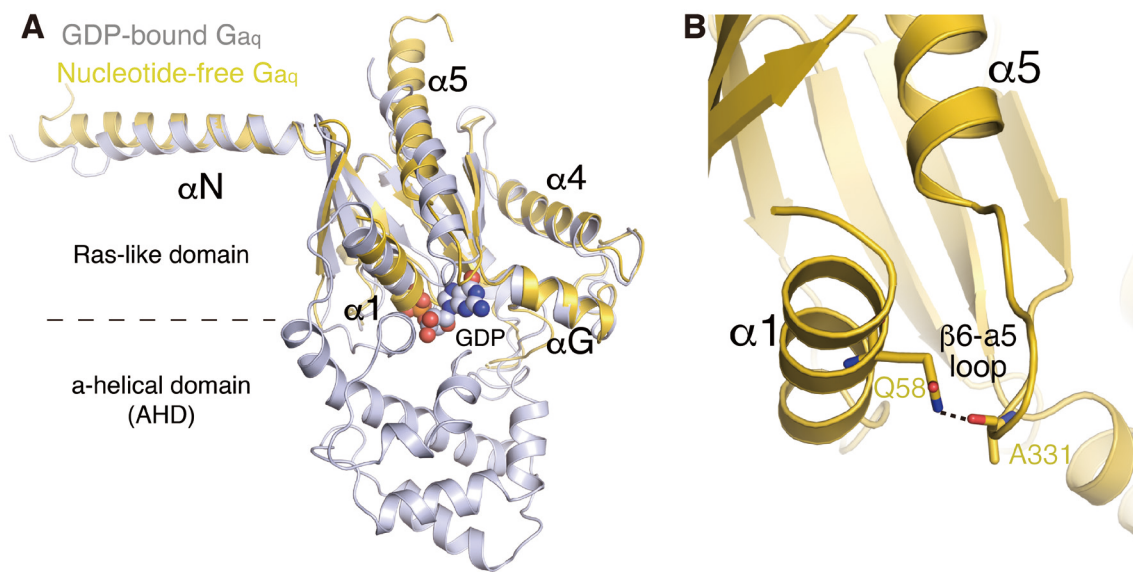


**Fig. S7. MIR engaged G11 structures.** **A.** Superposition of the nucleotide-free  $G\alpha_{11}$  onto the GDP-bound  $G\alpha_q$  (PDB code 3AH8). Bound GDP is depicted as spheres in  $G\alpha_q$ . **B.** A hydrogen bond is formed between Gln58 and Ala331 that connects the  $\alpha 1$  helix and the  $\beta 6$ - $\alpha 5$  loop.

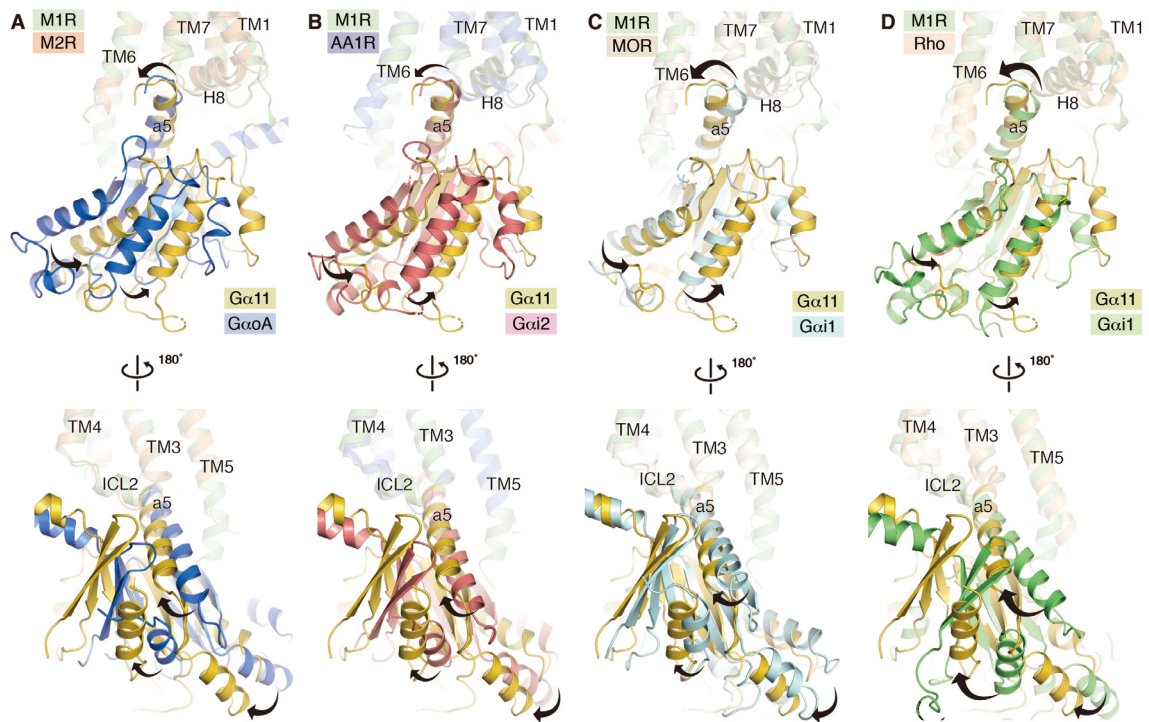


**Fig. S8. Comparison of the G-protein orientation between M1R-G<sub>11</sub> and GPCR-G<sub>i/o</sub> complexes.** Structure of each GPCR-G<sub>i/o</sub> complex was superposed onto M1R-G<sub>11</sub> based on the receptor component. **A.** M2R (this study), **B.** A1adenosine receptor (PDB ID: 6D9H), **C.** MOR (PDB ID: 6DDE), **D.** rhodopsin (PDB ID: 6CMO). Receptor structures are made transparent for clarity. The arrows indicate the relative orientation differences.

## Residues interacting with G11 in M1R-G11 structure

\* Residues reportedly important for the G-protein selectivity

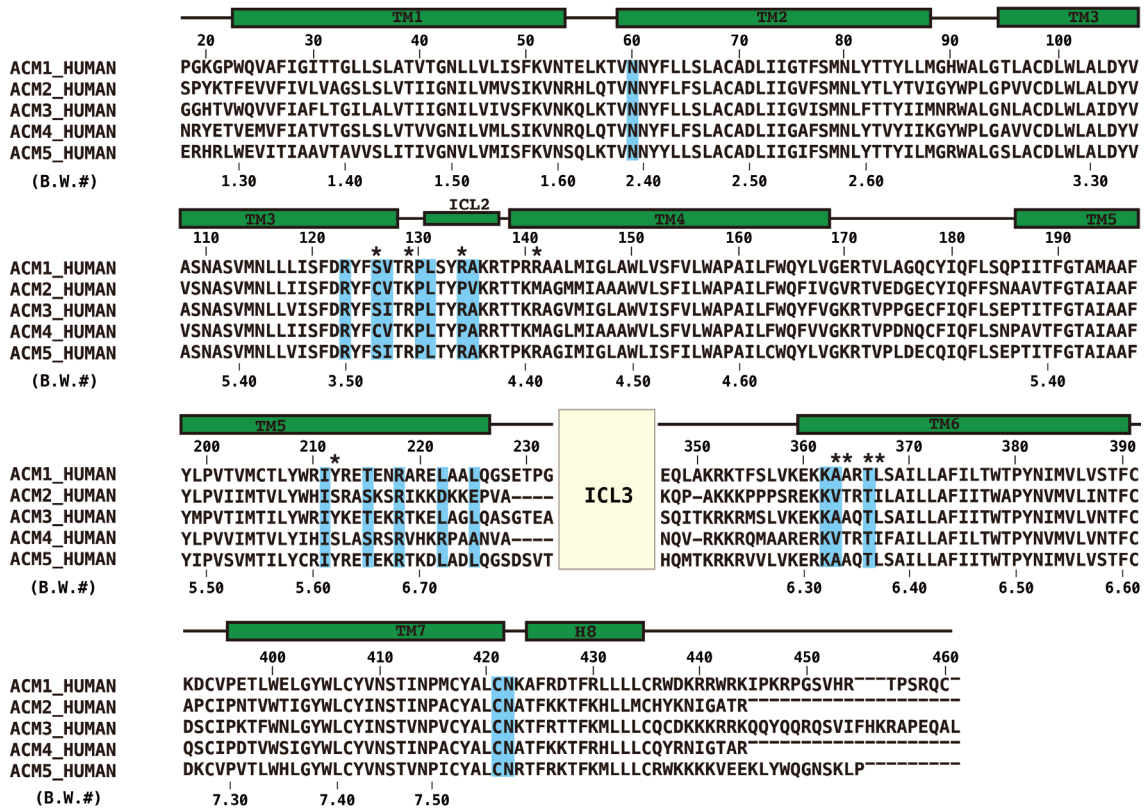


**Fig. S9. Sequence alignment of muscarinic receptors.** Residue numbers as well as the helical secondary structures are shown based on M1R. Ballesteros-Weinstein numbers are shown on the bottom of each row. The residues in M1R that interact with G<sub>11</sub> are highlighted in cyan. Those residues reportedly important for the G-protein selectivity are labeled with an asterisk.



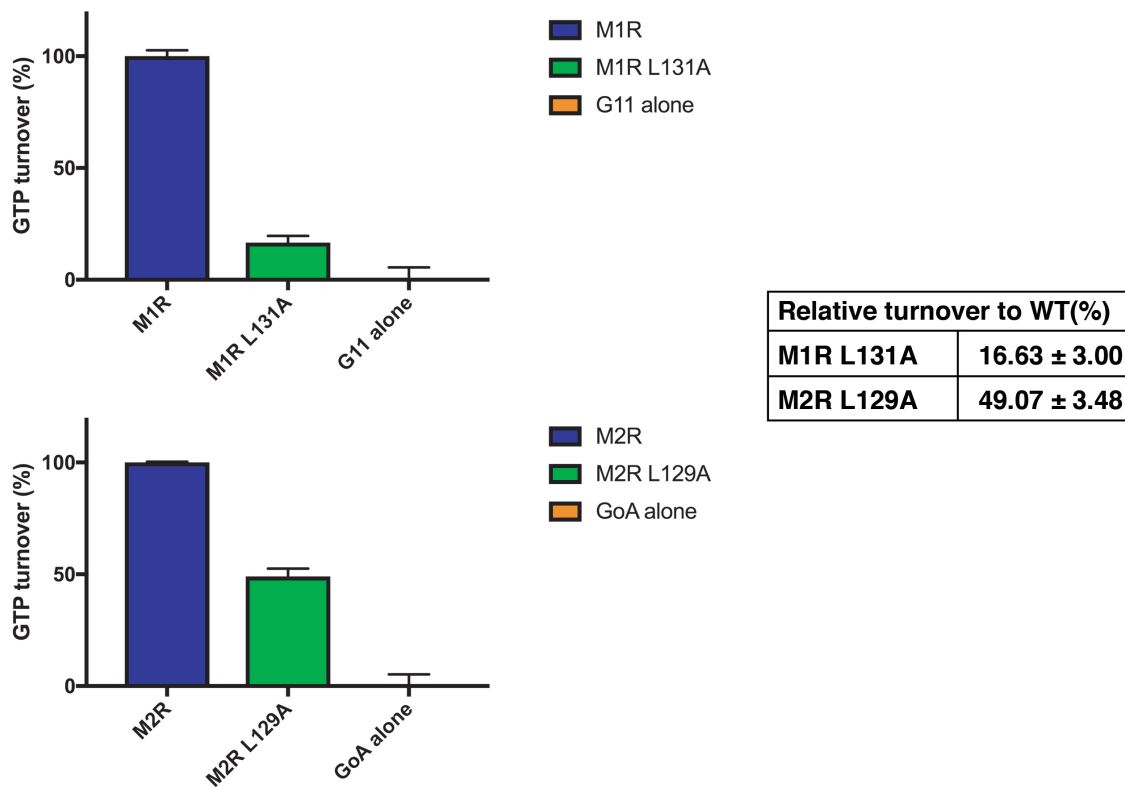


**Fig. S10. G-protein activation efficiency of ICL2 mutants.** Coupling of M1R or M2R with respective  $G_{11}$  or  $G_{oA}$  was measured by GTP turnover using WT receptors and Leu to Ala mutants in ICL2. Error bar denotes s.e.m. of four replicates. Values represent mean  $\pm$  s.e.m..

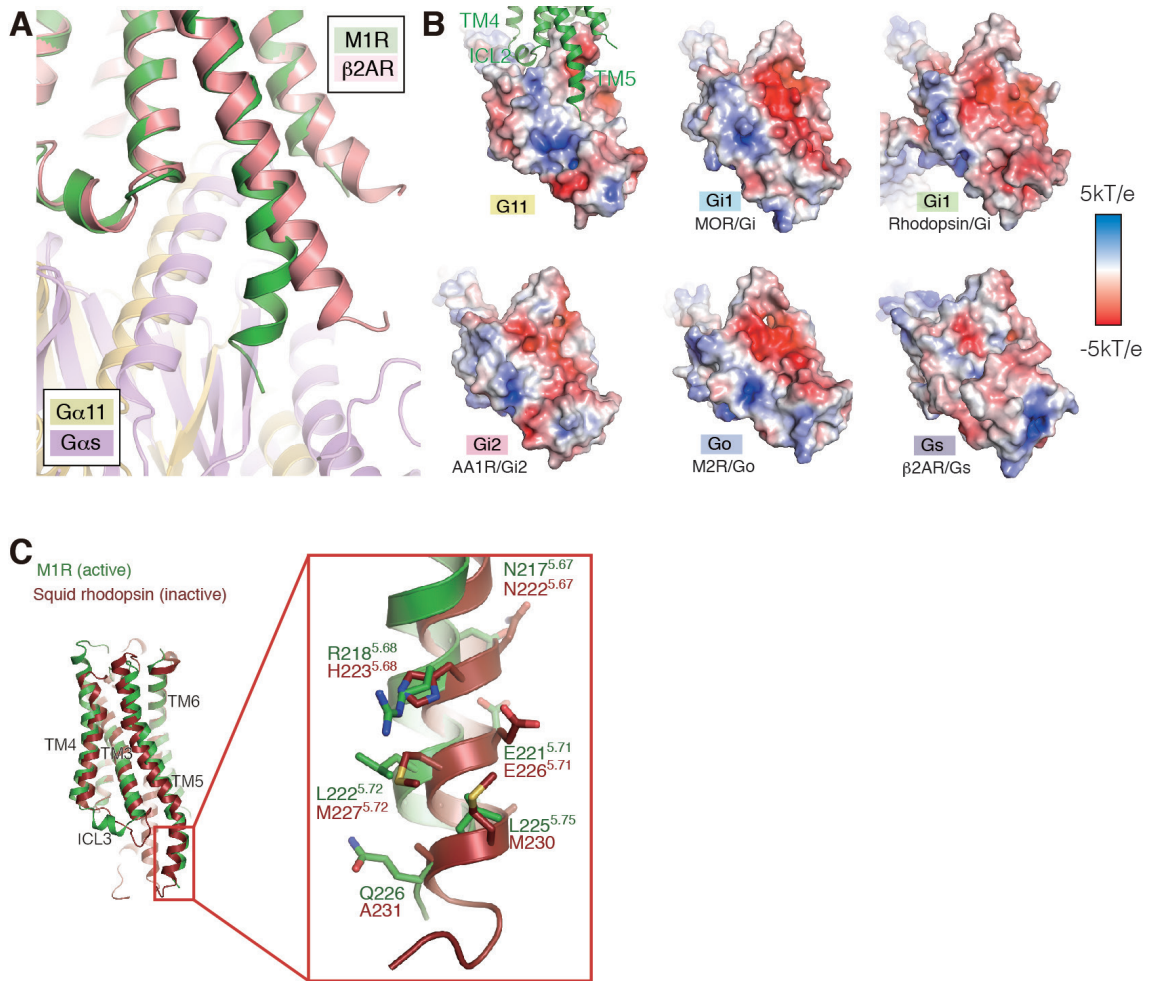


**Fig. S11. Hydrophobic nature of the interface between the TM5 extension and G11.**  
**A.** Comparison of the TM5 extension between M1R-G11 and  $\beta$ 2AR-Gs. **B.** Surface charge distribution of G<sub>11</sub>, G<sub>i/o</sub>, and G<sub>s</sub> around the interface between the extended TM5. Note that only G<sub>11</sub> has a neutral charge facing the extended TM5. **C.** Structural similarity of active M1R and inactive squid rhodopsin. Structure of the squid rhodopsin (dark brown: PDB ID: 2Z73) is superimposed on M1R (green). Residues in the TM5 extension are shown in an enlarged box.

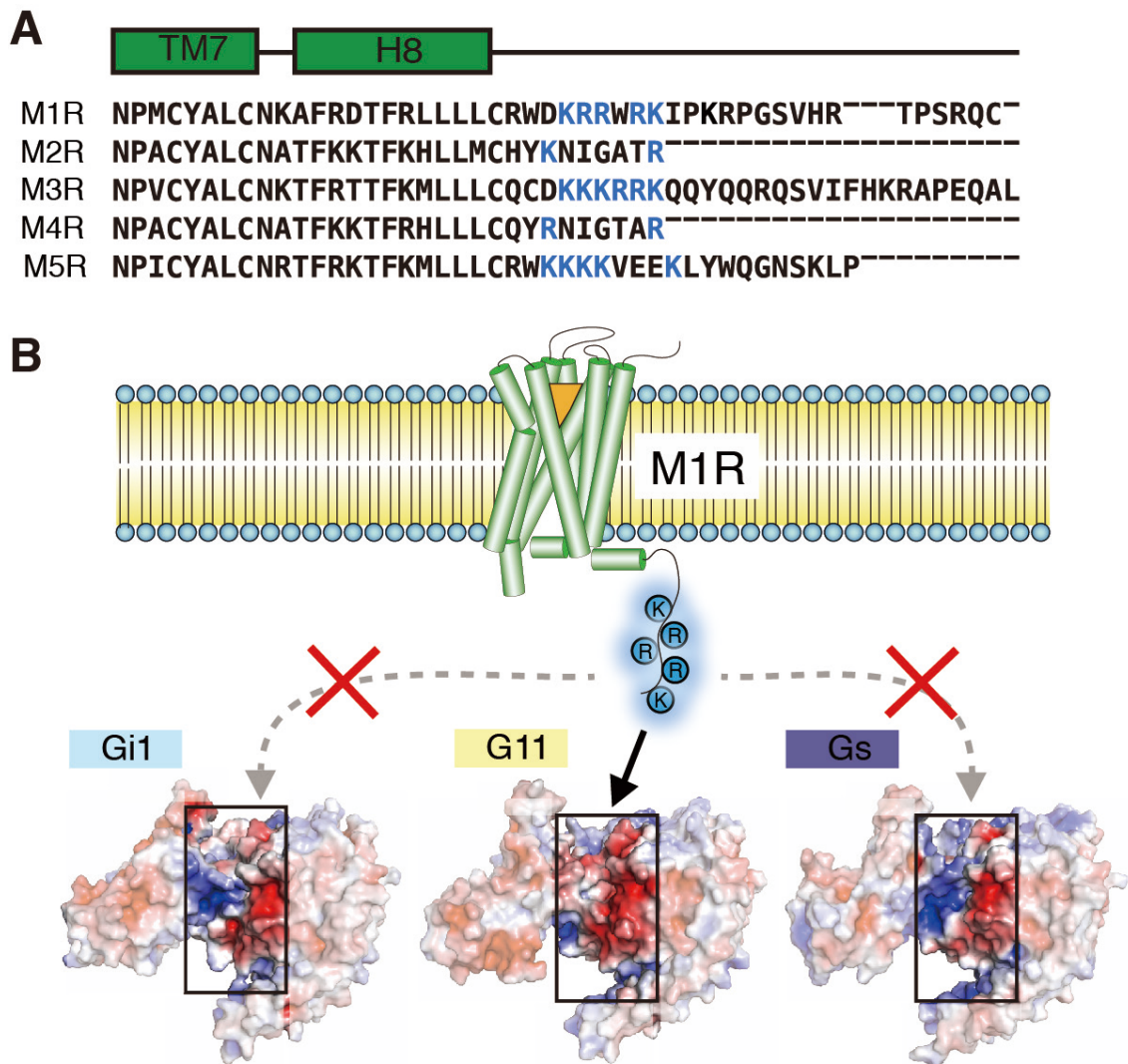


**Fig. S12. Interaction of the C-terminus of M1R with the G-protein interface. A.** Sequence alignment of muscarinic receptor family members at the C-terminus. Positively charged residues following H8 are colored in blue. **B.** Electrostatic surface potential of  $G_{i1}$ ,  $G_{11}$ , and  $G_s$  in their nucleotide-free form. Polybasic region in the C-tail of M1R interacts with  $G_{11}$  but not  $G_{i1}$  or  $G_s$  due to the positive environment of their interfaces.  $G\alpha/\beta$  subunit interfaces are highlighted in a rectangular box. PDB code used for the calculation is 6DDE for  $G_{i1}$ , 3SN6 for  $G_s$ .

## H8

5ht2a_human	QYK <b>ENKK</b> PLQLILVNTIPALAY <b>KSS</b>
5ht2b_human	TCNYR <b>ATKSVKTLRKRSSKIYFRNP</b>
5ht2c_human	NY <b>KVEKKPPVRQIPRVAATALSGRE</b>
acm1_human	C <b>RWDKRRWRKIPKRPGSVHRTPSRQ</b>
acm3_human	LCQCD <b>KKKRRKQQYQQRQSVIFHKR</b>
acm5_human	LC <b>RWKKKKVVEEKLYWQGN</b> SKLP---
adala_human	IQCLC <b>RKQSSKHALGYTLHPPSQAV</b>
adalb_human	CQ <b>CRGRRRRRRRRRRLGGCAYTYR</b>
adald_human	CQ <b>RRRRRRRPLWRVYGGHHWR</b> ASTS
hrh2_human	C <b>RLANRNSHK</b> TSL <b>R</b> SNASQL <b>SRTQS</b>
agtr1_human	PP <b>KAKSHSNLSTKMSTLSYR</b> PSDNV
nibr_human	G <b>RKSYQER</b> GTSYLLSSSAV <b>RMTSLK</b>
bkrb1_human	TP <b>KSLAP</b> ISS <b>SHRKEIFQLFWRN</b> --
nmur1_human	CLGACC <b>HRLRPRHSSHSLSR</b> MTTGS
ntr1_human	ACLCPVW <b>RRRRKRPAFSRK</b> ADSVSS
ntr2_human	SSLCGE <b>HHPMKRLPPKPQ</b> SPTLMDT
ox1r_human	SCCLPGLGPCGSL <b>KAPSPRSSASHK</b>
ox2r_human	SCCCLGV <b>HHRQEDRLTRGRT</b> STES <b>R</b>
nk1r_human	<b>RCCPF</b> ISAGDYEGLEM <b>KSTRYLQ</b> TQ
v1ar_human	PCCQNM <b>KEKFNKED</b> TDSMS <b>RRQ</b> TFY
v1br_human	ACCGGPQ <b>PMRRRLSDGSLSSRH</b> TT
oxyr_human	LCCSASYL <b>KGRRLGETSAS</b> KKSNSS
lpar3_human	CFSQEN <b>PERRPSRIPSTVLSR</b> SDTG
s1pr3_human	NCLV <b>RGRGARASPIQPALDPSRSKS</b>
p2ry1_human	<b>KASRRSEANLQSKSEDM</b> TLNILPEF
p2ry2_human	PTG <b>PSPATPARRRLGLRR</b> SDRTDMQ
gpr39_human	CC <b>RLSLQHANHEKRLRVHAH</b> STTDS
gpr75_human	YIGLGFF <b>CKQKTRLRAMGKGN</b> LEV

**Fig. S13. Polybasic cluster at the C-terminal tail in Gq-coupling GPCRs.** Sequence alignment of the C-terminal tail proximal to H8 of representative Gq-coupling GPCRs. Positively charged residues (K, R, H) are colored in blue.

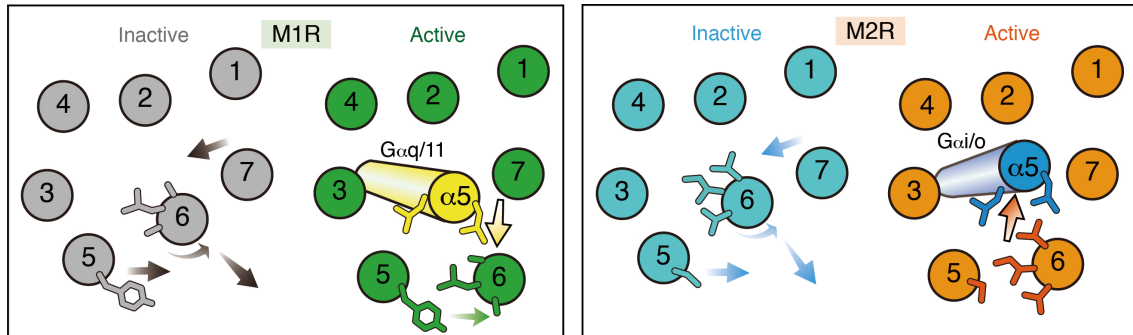


**Fig. S14. Schematic drawing of the distinct G-protein coupling model of M1R-G<sub>q/11</sub> and M2R-G<sub>i/o</sub>.** Amino acids reported to be the major determinants for coupling specificity in M1R and M2R are shown as sticks in TM5 and TM6. Note that most of these amino acids are involved in stabilizing the interaction between TM5 and TM6, and do not directly engaged with the G-protein.

A						B					
	5.62	6.33	6.34	6.37	6.38		5.62	6.33	6.34	6.37	6.38
5-HT2A receptor	I	A	C	L	G	5-HT1A receptor	F	T	V	L	G
5-HT2B receptor	I	A	S	L	G	5-HT1B receptor	Y	A	T	L	G
5-HT2C receptor	I	A	S	L	G	M2 receptor	S	V	T	I	L
M1 receptor	Y	A	A	L	S	M4 receptor	S	V	T	I	F
M3 receptor	Y	A	A	L	S	alpha 2A-adrenoceptor	Y	F	T	L	A
M5 receptor	Y	A	A	L	S	alpha 2B-adrenoceptor	Y	F	T	L	A
alpha1A-adrenoceptor	Y	A	A	L	G	D2 receptor	Y	A	T	L	A
alpha1B-adrenoceptor	Y	A	A	L	G	D4 receptor	F	A	M	L	P
alpha1D-adrenoceptor	Y	A	A	L	A	apelin receptor	A	L	L	I	V
H2 receptor	F	A	T	L	A	C5a1 receptor	L	T	L	V	V
TA1 receptor	Y	A	V	L	G	FPR1	A	P	L	L	S
AT1 receptor	W	I	F	I	M	FPR2/ALX	A	P	L	L	T
BB1 receptor	A	L	A	V	L	GAL1 receptor	L	T	A	V	L
BB2 receptor	A	L	A	V	L	GAL3 receptor	L	A	G	M	L
BB3 receptor	A	I	A	V	L	MCH1 receptor	L	V	T	A	I
B1 receptor	L	T	T	I	L	Y2 receptor	W	T	T	L	V
ETA receptor	T	V	A	V	F	delta; receptor	L	I	T	V	L
ghrelin receptor	G	T	V	L	A	kappa; receptor	I	I	T	V	L
GnRH1 receptor	I	T	L	T	V	mu; receptor	I	I	T	V	L
MCH2 receptor	L	L	T	V	L	NOP receptor	I	I	T	V	L
NMU1 receptor	G	V	T	L	F	SST1 receptor	I	I	T	V	M
NPS receptor	I	A	I	S	I	SST2 receptor	I	V	T	V	S
NTS1 receptor	A	G	V	L	R	SST3 receptor	V	V	T	V	V
NTS2 receptor	V	S	V	L	R	SST4 receptor	V	I	T	V	L
OX1 receptor	F	T	A	L	M	SST5 receptor	V	V	T	V	L
OX2 receptor	F	T	A	L	M	CCR1	I	A	V	I	F
NK1 receptor	G	V	V	M	I	CCR4	I	A	V	I	F
V1A receptor	C	T	V	T	F	CXCR4	I	A	L	T	V
V1B receptor	C	T	V	T	F	LPA1 receptor	F	L	L	V	V
OT receptor	S	T	V	T	F	S1P1 receptor	Y	L	L	V	I
FFA1 receptor	L	R	A	V	A	CB1 receptor	L	L	A	L	V
BLT1 receptor	G	T	G	V	V	A1 receptor	F	I	A	L	A
LPA2 receptor	F	L	V	V	V	A3 receptor	F	T	A	L	F
LPA3 receptor	Y	L	M	V	M						
S1P3 receptor	Y	L	L	V	V						
P2Y1 receptor	V	K	S	L	V						
P2Y2 receptor	A	K	S	T	I						
P2Y4 receptor	A	R	S	T	I						
GPR39	W	T	I	L	R						
GPR75	A	A	V	C	V						

**Fig. S15. Alignment of the amino acid residues critical for the G-protein selectivity in mAChRs (Ballesteros-Weinstein. numbers: 5.62, 6.33, 6.34, 6.37, and 6.38).**

Alignment of the selected residues among representative **A.** Gq/11-coupling GPCRs **B.** Gi/o-coupling GPCRs.

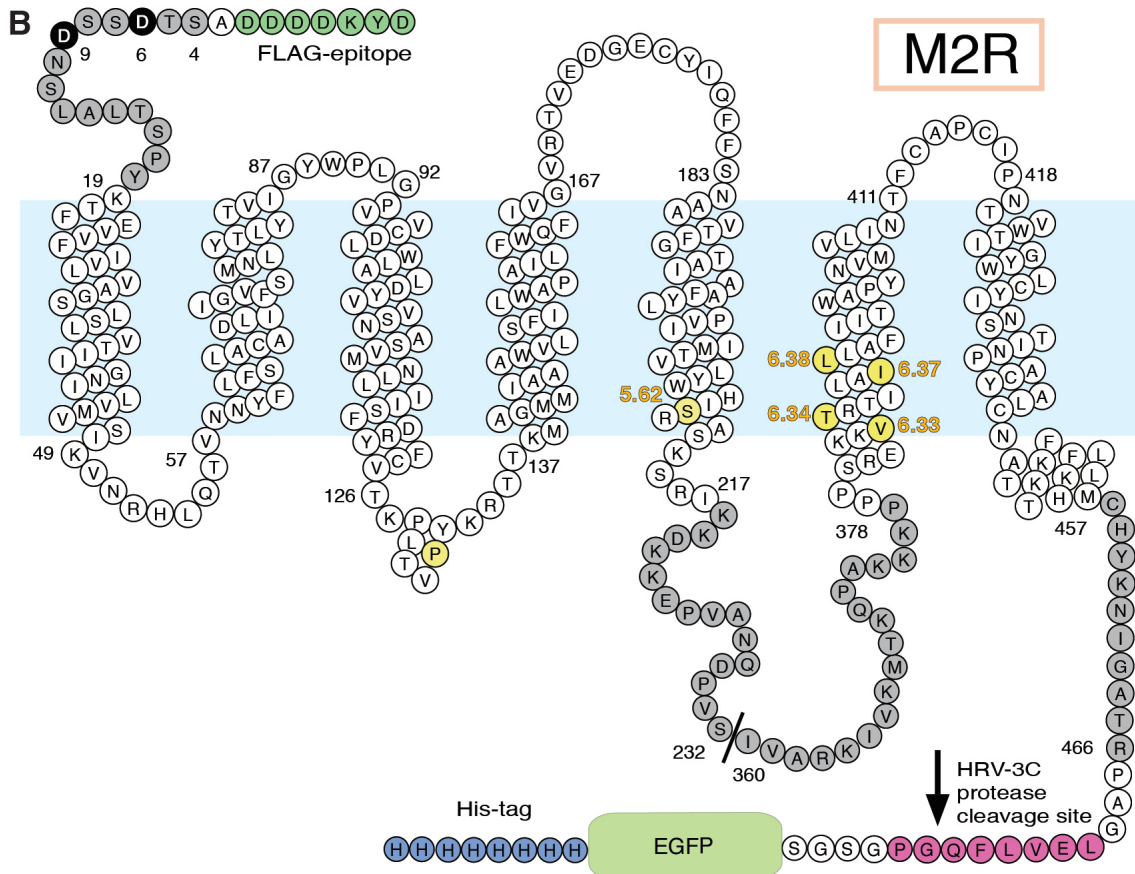
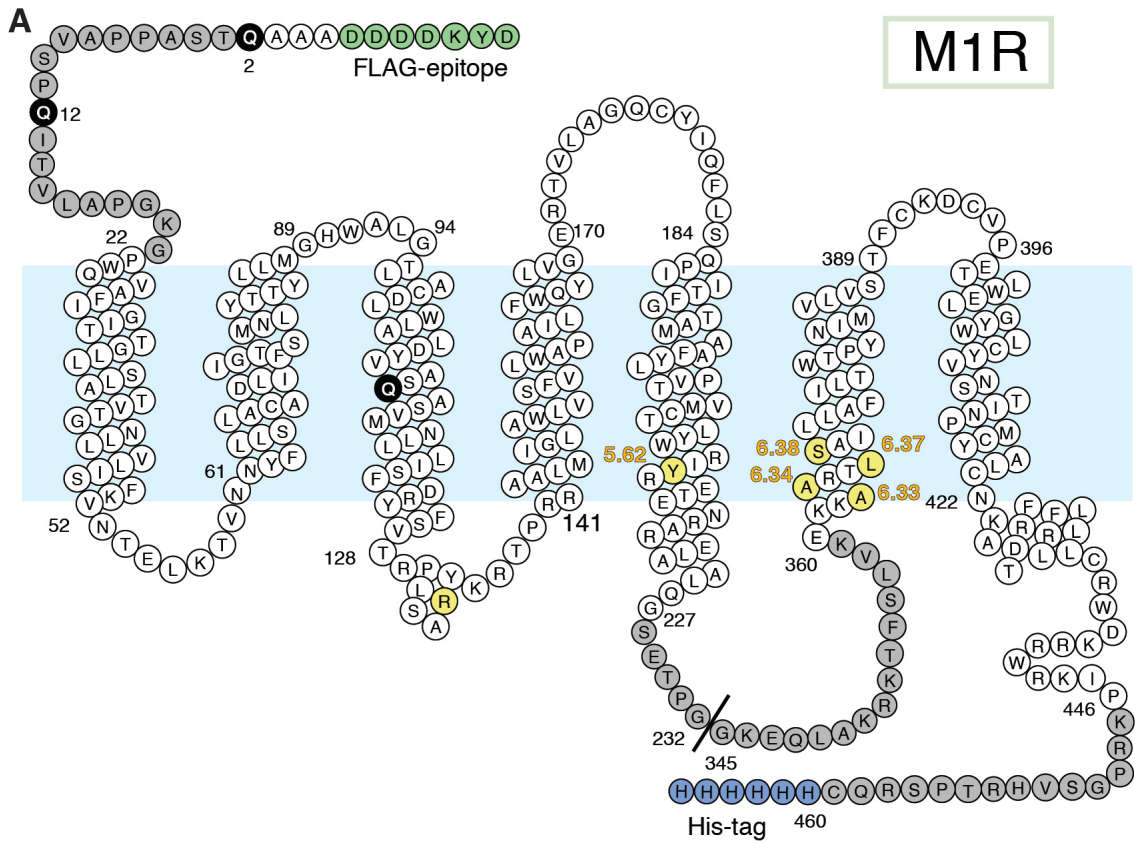


**Fig. S16. Schematic diagram of receptor constructs used in this study.** **A.** Diagram of the M1R construct used in the structural study. Two N-linked glycosylation sites (N2, N12) were eliminated by mutating to glutamine (Q). N110 located in TM3 was unintentionally mutated to glutamine. Unresolved residues are colored in grey. **B.** Diagram of the M2R construct. Two N-linked glycosylation sites (N6, N9) were eliminated by mutating to aspartic acid (D). Unresolved residues are colored in grey. The residues reportedly important for the G-protein selectivity are highlighted in yellow and labeled with the Ballesteros-Weinstein numbers.



	M1R/G <sub>111</sub> N/scFv16	M2R/G <sub>0A1</sub> N/scFv16
Data collection and processing		
Magnification	130,000	130,000
Voltage (kV)	300	300
Electron exposure (e-/Å <sup>2</sup> )	56	56
Defocus range (μm)	-1.0~-2.0	-1.0~-2.0
Pixel size (Å)	1.06	1.06
Symmetry imposed	C1	C1
Final particle images (no.)	277,988	261,730
Map resolution (Å)	3.3	3.6
FSC threshold	0.143	0.143
Refinement		
Initial model used (PDB code)	4MQS	4MQS
Map sharpening B-factor (Å <sup>2</sup> )	-116	-135
Model composition		
Non-hydrogen atoms	9051	8744
Protein residues	1152	1129
B-factors (Å <sup>2</sup> )		
Protein	124.94	138.66
R.m.s. deviations		
Bond lengths (Å)	0.007	0.009
Bond angles (°)	0.962	1.062
Validation		
MolProbity score	1.67	1.92
Clashscore	6.07	8.18
Poor rotamers (%)	0.84	1.17
Ramachandran plot		
Favored (%)	95.15	93.52
Allowed (%)	4.85	6.48
Disallowed (%)	0.00	0.00

**Table S1. Cryo-EM data Collection, refinement and validation statistics**

	Area_SA/A <sup>2</sup>	Area_MS/A <sup>2</sup>	Vol_SA/A <sup>3</sup>	Vol_MS/A <sup>3</sup>
M1R(G11 engaged)	192.4	536.7	73.7	595.2
M2R(GoA engaged)	186.6	583.9	55.0	620.7

**Table S2. Analysis of the orthosteric binding pocket in the M1R and M2R.** Solvent accessible (SA) and molecular surface (MS) volume and area are analyzed using CASTp 3.0 server(26). Solvent radius of 1.5 is used in this analysis.

**NMS (Kd: nM)**

<b>M1R_ΔICL3_N110Q</b>	<b>0.25 ± 0.03</b>
<b>M1R_wild-type_full-length</b>	<b>0.30 ± 0.06</b>
<b>M1R_ΔICL3</b>	<b>0.39 ± 0.05</b>

**Iperoxo (-LogKi)**

<b>M1R_ΔICL3_N110Q</b>	<b>5.67 ± 0.10</b>
<b>M1R_wild-type_full-length</b>	<b>5.27 ± 0.06</b>
<b>M1R_ΔICL3</b>	<b>5.23 ± 0.03</b>

**Table S3. Pharmacology of M1R constructs.** Truncation of ICL3 or mutation of N110Q does not affect the affinity constant for NMS or iperoxo. Values represent mean ± s.e.m. of three separate experiments performed in triplicate.

## References and Notes

1. J. Wess, Muscarinic acetylcholine receptor knockout mice: Novel phenotypes and clinical implications. *Annu. Rev. Pharmacol. Toxicol.* **44**, 423–450 (2004).  
[doi:10.1146/annurev.pharmtox.44.101802.121622](https://doi.org/10.1146/annurev.pharmtox.44.101802.121622) [Medline](#)
2. C. J. Langmead, J. Watson, C. Reavill, Muscarinic acetylcholine receptors as CNS drug targets. *Pharmacol. Ther.* **117**, 232–243 (2008).  
[doi:10.1016/j.pharmthera.2007.09.009](https://doi.org/10.1016/j.pharmthera.2007.09.009) [Medline](#)
3. E. P. Lebois, C. Thorn, J. R. Edgerton, M. Popiolek, S. Xi, Muscarinic receptor subtype distribution in the central nervous system and relevance to aging and Alzheimer's disease. *Neuropharmacology* **136**, 362–373 (2018).  
[doi:10.1016/j.neuropharm.2017.11.018](https://doi.org/10.1016/j.neuropharm.2017.11.018) [Medline](#)
4. M. Thomsen, G. Sørensen, D. Dencker, Physiological roles of CNS muscarinic receptors gained from knockout mice. *Neuropharmacology* **136**, 411–420 (2018). [doi:10.1016/j.neuropharm.2017.09.011](https://doi.org/10.1016/j.neuropharm.2017.09.011) [Medline](#)
5. K. Haga, A. C. Kruse, H. Asada, T. Yurugi-Kobayashi, M. Shiroishi, C. Zhang, W. I. Weis, T. Okada, B. K. Kobilka, T. Haga, T. Kobayashi, Structure of the human M2 muscarinic acetylcholine receptor bound to an antagonist. *Nature* **482**, 547–551 (2012). [doi:10.1038/nature10753](https://doi.org/10.1038/nature10753) [Medline](#)
6. A. C. Kruse, J. Hu, A. C. Pan, D. H. Arlow, D. M. Rosenbaum, E. Rosemond, H. F. Green, T. Liu, P. S. Chae, R. O. Dror, D. E. Shaw, W. I. Weis, J. Wess, B. K. Kobilka, Structure and dynamics of the M3 muscarinic acetylcholine receptor. *Nature* **482**, 552–556 (2012). [doi:10.1038/nature10867](https://doi.org/10.1038/nature10867) [Medline](#)
7. D. M. Thal, B. Sun, D. Feng, V. Nawaratne, K. Leach, C. C. Felder, M. G. Bures, D. A. Evans, W. I. Weis, P. Bachhawat, T. S. Kobilka, P. M. Sexton, B. K. Kobilka, A. Christopoulos, Crystal structures of the M1 and M4 muscarinic acetylcholine receptors. *Nature* **531**, 335–340 (2016). [doi:10.1038/nature17188](https://doi.org/10.1038/nature17188) [Medline](#)
8. A. C. Kruse, A. M. Ring, A. Manglik, J. Hu, K. Hu, K. Eitel, H. Hübner, E. Pardon, C. Valant, P. M. Sexton, A. Christopoulos, C. C. Felder, P. Gmeiner, J. Steyaert, W. I. Weis, K. C. Garcia, J. Wess, B. K. Kobilka, Activation and allosteric

- modulation of a muscarinic acetylcholine receptor. *Nature* **504**, 101–106 (2013).  
[doi:10.1038/nature12735](https://doi.org/10.1038/nature12735) [Medline](#)
9. H.-W. Choe, Y. J. Kim, J. H. Park, T. Morizumi, E. F. Pai, N. Krauss, K. P. Hofmann, P. Scheerer, O. P. Ernst, Crystal structure of metarhodopsin II. *Nature* **471**, 651–655 (2011). [doi:10.1038/nature09789](https://doi.org/10.1038/nature09789) [Medline](#)
10. S. G. F. Rasmussen, B. T. DeVree, Y. Zou, A. C. Kruse, K. Y. Chung, T. S. Kobilka, F. S. Thian, P. S. Chae, E. Pardon, D. Calinski, J. M. Mathiesen, S. T. A. Shah, J. A. Lyons, M. Caffrey, S. H. Gellman, J. Steyaert, G. Skiniotis, W. I. Weis, R. K. Sunahara, B. K. Kobilka, Crystal structure of the  $\beta_2$  adrenergic receptor-Gs protein complex. *Nature* **477**, 549–555 (2011).  
[doi:10.1038/nature10361](https://doi.org/10.1038/nature10361) [Medline](#)
11. B. Carpenter, R. Nehmé, T. Warne, A. G. W. Leslie, C. G. Tate, Structure of the adenosine A(2A) receptor bound to an engineered G protein. *Nature* **536**, 104–107 (2016). [doi:10.1038/nature18966](https://doi.org/10.1038/nature18966) [Medline](#)
12. T. Flock, A. S. Hauser, N. Lund, D. E. Gloriam, S. Balaji, M. M. Babu, Selectivity determinants of GPCR-G-protein binding. *Nature* **545**, 317–322 (2017).  
[doi:10.1038/nature22070](https://doi.org/10.1038/nature22070) [Medline](#)
13. Y. Zhang, B. Sun, D. Feng, H. Hu, M. Chu, Q. Qu, J. T. Tarrasch, S. Li, T. Sun Kobilka, B. K. Kobilka, G. Skiniotis, Cryo-EM structure of the activated GLP-1 receptor in complex with a G protein. *Nature* **546**, 248–253 (2017).  
[doi:10.1038/nature22394](https://doi.org/10.1038/nature22394) [Medline](#)
14. Y.-L. Liang, M. Khoshouei, M. Radjainia, Y. Zhang, A. Glukhova, J. Tarrasch, D. M. Thal, S. G. B. Furness, G. Christopoulos, T. Coudrat, R. Danev, W. Baumeister, L. J. Miller, A. Christopoulos, B. K. Kobilka, D. Wootten, G. Skiniotis, P. M. Sexton, Phase-plate cryo-EM structure of a class B GPCR-G-protein complex. *Nature* **546**, 118–123 (2017). [doi:10.1038/nature22327](https://doi.org/10.1038/nature22327)  
[Medline](#)
15. A. Koehl, H. Hu, S. Maeda, Y. Zhang, Q. Qu, J. M. Paggi, N. R. Latorraca, D. Hilger, R. Dawson, H. Matile, G. F. X. Schertler, S. Granier, W. I. Weis, R. O. Dror, A. Manglik, G. Skiniotis, B. K. Kobilka, Structure of the  $\mu$ -opioid

- receptor-G<sub>i</sub> protein complex. *Nature* **558**, 547–552 (2018). [doi:10.1038/s41586-018-0219-7](https://doi.org/10.1038/s41586-018-0219-7) [Medline](#)
16. Y. Kang, O. Kuybeda, P. W. de Waal, S. Mukherjee, N. Van Eps, P. Dutka, X. E. Zhou, A. Bartesaghi, S. Erramilli, T. Morizumi, X. Gu, Y. Yin, P. Liu, Y. Jiang, X. Meng, G. Zhao, K. Melcher, O. P. Ernst, A. A. Kossiakoff, S. Subramaniam, H. E. Xu, Cryo-EM structure of human rhodopsin bound to an inhibitory G protein. *Nature* **558**, 553–558 (2018). [doi:10.1038/s41586-018-0215-y](https://doi.org/10.1038/s41586-018-0215-y) [Medline](#)
17. C. J. Draper-Joyce, M. Khoshouei, D. M. Thal, Y.-L. Liang, A. T. N. Nguyen, S. G. B. Furness, H. Venugopal, J.-A. Baltos, J. M. Plitzko, R. Danev, W. Baumeister, L. T. May, D. Wootten, P. M. Sexton, A. Glukhova, A. Christopoulos, Structure of the adenosine-bound human adenosine A<sub>1</sub> receptor-G<sub>i</sub> complex. *Nature* **558**, 559–563 (2018). [doi:10.1038/s41586-018-0236-6](https://doi.org/10.1038/s41586-018-0236-6) [Medline](#)
18. J. García-Nafría, R. Nehmé, P. C. Edwards, C. G. Tate, Cryo-EM structure of the serotonin 5-HT<sub>1B</sub> receptor coupled to heterotrimeric G<sub>o</sub>. *Nature* **558**, 620–623 (2018). [doi:10.1038/s41586-018-0241-9](https://doi.org/10.1038/s41586-018-0241-9) [Medline](#)
19. S. Maeda, A. Koehl, H. Matile, H. Hu, D. Hilger, G. F. X. Schertler, A. Manglik, G. Skiniotis, R. J. P. Dawson, B. K. Kobilka, Development of an antibody fragment that stabilizes GPCR/G-protein complexes. *Nat. Commun.* **9**, 3712 (2018). [doi:10.1038/s41467-018-06002-w](https://doi.org/10.1038/s41467-018-06002-w) [Medline](#)
20. J. A. Ballesteros, H. Weinstein, in *Receptor Molecular Biology*, S. C. Sealfon, Ed. (Academic Press, 1995), vol. 25 of *Methods in Neurosciences*, pp. 366–428.
21. A. A. Jensen, T. A. Spalding, Allosteric modulation of G-protein coupled receptors. *Eur. J. Pharm. Sci.* **21**, 407–420 (2004). [doi:10.1016/j.ejps.2003.11.007](https://doi.org/10.1016/j.ejps.2003.11.007) [Medline](#)
22. R. O. Dror, H. F. Green, C. Valant, D. W. Borhani, J. R. Valcourt, A. C. Pan, D. H. Arlow, M. Canals, J. R. Lane, R. Rahmani, J. B. Baell, P. M. Sexton, A. Christopoulos, D. E. Shaw, Structural basis for modulation of a G-protein-coupled receptor by allosteric drugs. *Nature* **503**, 295–299 (2013). [doi:10.1038/nature12595](https://doi.org/10.1038/nature12595) [Medline](#)
23. R. O. Dror, T. J. Mildorf, D. Hilger, A. Manglik, D. W. Borhani, D. H. Arlow, A. Philippsen, N. Villanueva, Z. Yang, M. T. Lerch, W. L. Hubbell, B. K. Kobilka,

- R. K. Sunahara, D. E. Shaw, Structural basis for nucleotide exchange in heterotrimeric G proteins. *Science* **348**, 1361–1365 (2015).  
[doi:10.1126/science.aaa5264](https://doi.org/10.1126/science.aaa5264) [Medline](#)
24. G. J. Digby, M. J. Noetzel, M. Bubser, T. J. Utley, A. G. Walker, N. E. Byun, E. P. Lebois, Z. Xiang, D. J. Sheffler, H. P. Cho, A. A. Davis, N. E. Nemirovsky, S. E. Mennenga, B. W. Camp, H. A. Bimonte-Nelson, J. Bode, K. Italiano, R. Morrison, J. S. Daniels, C. M. Niswender, M. F. Olive, C. W. Lindsley, C. K. Jones, P. J. Conn, Novel allosteric agonists of M1 muscarinic acetylcholine receptors induce brain region-specific responses that correspond with behavioral effects in animal models. *J. Neurosci.* **32**, 8532–8544 (2012).  
[doi:10.1523/JNEUROSCI.0337-12.2012](https://doi.org/10.1523/JNEUROSCI.0337-12.2012) [Medline](#)
25. R. Schrage, J. Holze, J. Klöckner, A. Balkow, A. S. Klause, A.-L. Schmitz, M. De Amici, E. Kostenis, C. Tränkle, U. Holzgrabe, K. Mohr, New insight into active muscarinic receptors with the novel radioagonist [<sup>3</sup>H]iperoxo. *Biochem. Pharmacol.* **90**, 307–319 (2014). [doi:10.1016/j.bcp.2014.05.012](https://doi.org/10.1016/j.bcp.2014.05.012) [Medline](#)
26. W. Tian, C. Chen, X. Lei, J. Zhao, J. Liang, CASTp 3.0: Computed atlas of surface topography of proteins. *Nucleic Acids Res.* **46**, W363–W367 (2018).  
[doi:10.1093/nar/gky473](https://doi.org/10.1093/nar/gky473) [Medline](#)
27. N. Van Eps, C. Altenbach, L. N. Caro, N. R. Latorraca, S. A. Hollingsworth, R. O. Dror, O. P. Ernst, W. L. Hubbell, G<sub>i</sub>- and G<sub>s</sub>-coupled GPCRs show different modes of G-protein binding. *Proc. Natl. Acad. Sci. U.S.A.* **115**, 2383–2388 (2018). [Medline](#)
28. A. I. Kaya, A. D. Lokits, J. A. Gilbert, T. M. Iverson, J. Meiler, H. E. Hamm, A conserved phenylalanine as a relay between the α5 helix and the GDP binding region of heterotrimeric G<sub>i</sub> protein α subunit. *J. Biol. Chem.* **289**, 24475–24487 (2014). [doi:10.1074/jbc.M114.572875](https://doi.org/10.1074/jbc.M114.572875) [Medline](#)
29. A. Nishimura, K. Kitano, J. Takasaki, M. Taniguchi, N. Mizuno, K. Tago, T. Hakoshima, H. Itoh, Structural basis for the specific inhibition of heterotrimeric G<sub>q</sub> protein by a small molecule. *Proc. Natl. Acad. Sci. U.S.A.* **107**, 13666–13671 (2010). [doi:10.1073/pnas.1003553107](https://doi.org/10.1073/pnas.1003553107) [Medline](#)

30. V. M. Tesmer, T. Kawano, A. Shankaranarayanan, T. Kozasa, J. J. G. Tesmer, Snapshot of activated G proteins at the membrane: The Galphaq-GRK2-Gbetagamma complex. *Science* **310**, 1686–1690 (2005).  
[doi:10.1126/science.1118890](https://doi.org/10.1126/science.1118890) [Medline](#)
31. N. Kapoor, S. T. Menon, R. Chauhan, P. Sachdev, T. P. Sakmar, Structural evidence for a sequential release mechanism for activation of heterotrimeric G proteins. *J. Mol. Biol.* **393**, 882–897 (2009). [doi:10.1016/j.jmb.2009.08.043](https://doi.org/10.1016/j.jmb.2009.08.043) [Medline](#)
32. N. Blin, J. Yun, J. Wess, Mapping of single amino acid residues required for selective activation of Gq/11 by the m3 muscarinic acetylcholine receptor. *J. Biol. Chem.* **270**, 17741–17748 (1995). [doi:10.1074/jbc.270.30.17741](https://doi.org/10.1074/jbc.270.30.17741) [Medline](#)
33. O. Moro, J. Lamah, P. Högger, W. Sadée, Hydrophobic amino acid in the i2 loop plays a key role in receptor-G protein coupling. *J. Biol. Chem.* **268**, 22273–22276 (1993). [Medline](#)
34. O. Moro, M. S. Shockley, J. Lamah, W. Sadée, Overlapping multi-site domains of the muscarinic cholinergic Hm1 receptor involved in signal transduction and sequestration. *J. Biol. Chem.* **269**, 6651–6655 (1994). [Medline](#)
35. X. P. Chen, W. Yang, Y. Fan, J. S. Luo, K. Hong, Z. Wang, J. F. Yan, X. Chen, J. X. Lu, J. L. Benovic, N. M. Zhou, Structural determinants in the second intracellular loop of the human cannabinoid CB1 receptor mediate selective coupling to G(s) and G(i). *Br. J. Pharmacol.* **161**, 1817–1834 (2010).  
[doi:10.1111/j.1476-5381.2010.01006.x](https://doi.org/10.1111/j.1476-5381.2010.01006.x) [Medline](#)
36. A. S. Rose, M. Elgeti, U. Zachariae, H. Grubmüller, K. P. Hofmann, P. Scheerer, P. W. Hildebrand, Position of transmembrane helix 6 determines receptor G protein coupling specificity. *J. Am. Chem. Soc.* **136**, 11244–11247 (2014).  
[doi:10.1021/ja5055109](https://doi.org/10.1021/ja5055109) [Medline](#)
37. G. Pándy-Szekeres, C. Munk, T. M. Tsonkov, S. Mordalski, K. Harpsøe, A. S. Hauser, A. J. Bojarski, D. E. Gloriam, GPCRdb in 2018: Adding GPCR structure models and ligands. *Nucleic Acids Res.* **46** (D1), D440–D446 (2018).  
[doi:10.1093/nar/gkx1109](https://doi.org/10.1093/nar/gkx1109) [Medline](#)



38. M. Koyanagi, A. Terakita, Gq-coupled rhodopsin subfamily composed of invertebrate visual pigment and melanopsin. *Photochem. Photobiol.* **84**, 1024–1030 (2008). [doi:10.1111/j.1751-1097.2008.00369.x](https://doi.org/10.1111/j.1751-1097.2008.00369.x) [Medline](#)
39. M. Murakami, T. Kouyama, Crystal structure of squid rhodopsin. *Nature* **453**, 363–367 (2008). [doi:10.1038/nature06925](https://doi.org/10.1038/nature06925) [Medline](#)
40. K. Qin, C. Dong, G. Wu, N. A. Lambert, Inactive-state preassembly of G(q)-coupled receptors and G(q) heterotrimers. *Nat. Chem. Biol.* **7**, 740–747 (2011). [doi:10.1038/nchembio.642](https://doi.org/10.1038/nchembio.642) [Medline](#)
41. T. Kubo, H. Bujo, I. Akiba, J. Nakai, M. Mishina, S. Numa, Location of a region of the muscarinic acetylcholine receptor involved in selective effector coupling. *FEBS Lett.* **241**, 119–125 (1988). [doi:10.1016/0014-5793\(88\)81043-3](https://doi.org/10.1016/0014-5793(88)81043-3) [Medline](#)
42. J. Wess, M. R. Brann, T. I. Bonner, Identification of a small intracellular region of the muscarinic m3 receptor as a determinant of selective coupling to PI turnover. *FEBS Lett.* **258**, 133–136 (1989). [doi:10.1016/0014-5793\(89\)81633-3](https://doi.org/10.1016/0014-5793(89)81633-3) [Medline](#)
43. J. Lechleiter, R. Hellmiss, K. Duerson, D. Ennulat, N. David, D. Clapham, E. Peralta, Distinct sequence elements control the specificity of G protein activation by muscarinic acetylcholine receptor subtypes. *EMBO J.* **9**, 4381–4390 (1990). [doi:10.1002/j.1460-2075.1990.tb07888.x](https://doi.org/10.1002/j.1460-2075.1990.tb07888.x) [Medline](#)
44. J. Wess, T. I. Bonner, F. Dörje, M. R. Brann, Delineation of muscarinic receptor domains conferring selectivity of coupling to guanine nucleotide-binding proteins and second messengers. *Mol. Pharmacol.* **38**, 517–523 (1990). [Medline](#)
45. K. Blüml, E. Mutschler, J. Wess, Insertion mutagenesis as a tool to predict the secondary structure of a muscarinic receptor domain determining specificity of G-protein coupling. *Proc. Natl. Acad. Sci. U.S.A.* **91**, 7980–7984 (1994). [doi:10.1073/pnas.91.17.7980](https://doi.org/10.1073/pnas.91.17.7980) [Medline](#)
46. K. Blüml, E. Mutschler, J. Wess, Identification of an intracellular tyrosine residue critical for muscarinic receptor-mediated stimulation of phosphatidylinositol hydrolysis. *J. Biol. Chem.* **269**, 402–405 (1994). [Medline](#)

47. K. Blüml, E. Mutschler, J. Wess, Functional role of a cytoplasmic aromatic amino acid in muscarinic receptor-mediated activation of phospholipase C. *J. Biol. Chem.* **269**, 11537–11541 (1994). [Medline](#)
48. J. Liu, B. R. Conklin, N. Blin, J. Yun, J. Wess, Identification of a receptor/G-protein contact site critical for signaling specificity and G-protein activation. *Proc. Natl. Acad. Sci. U.S.A.* **92**, 11642–11646 (1995). [doi:10.1073/pnas.92.25.11642](https://doi.org/10.1073/pnas.92.25.11642) [Medline](#)
49. D. Singer-Lahat, J. Liu, J. Wess, C. C. Felder, The third intracellular domain of the m3 muscarinic receptor determines coupling to calcium influx in transfected Chinese hamster ovary cells. *FEBS Lett.* **386**, 51–54 (1996). [doi:10.1016/0014-5793\(96\)00398-5](https://doi.org/10.1016/0014-5793(96)00398-5) [Medline](#)
50. J. Liu, N. Blin, B. R. Conklin, J. Wess, Molecular mechanisms involved in muscarinic acetylcholine receptor-mediated G protein activation studied by insertion mutagenesis. *J. Biol. Chem.* **271**, 6172–6178 (1996). [doi:10.1074/jbc.271.11.6172](https://doi.org/10.1074/jbc.271.11.6172) [Medline](#)
51. E. Kostenis, J. Gomeza, C. Lerche, J. Wess, Genetic analysis of receptor-G $\alpha$  coupling selectivity. *J. Biol. Chem.* **272**, 23675–23681 (1997). [doi:10.1074/jbc.272.38.23675](https://doi.org/10.1074/jbc.272.38.23675) [Medline](#)
52. E. Kostenis, B. R. Conklin, J. Wess, Molecular basis of receptor/G protein coupling selectivity studied by coexpression of wild type and mutant m2 muscarinic receptors with mutant G  $\alpha$ (q) subunits. *Biochemistry* **36**, 1487–1495 (1997). [doi:10.1021/bi962554d](https://doi.org/10.1021/bi962554d) [Medline](#)
53. J. Wess, J. Liu, N. Blin, J. Yun, C. Lerche, E. Kostenis, Structural basis of receptor/G protein coupling selectivity studied with muscarinic receptors as model systems. *Life Sci.* **60**, 1007–1014 (1997). [doi:10.1016/S0024-3205\(97\)00041-6](https://doi.org/10.1016/S0024-3205(97)00041-6) [Medline](#)
54. B. R. Conklin, Z. Farfel, K. D. Lustig, D. Julius, H. R. Bourne, Substitution of three amino acids switches receptor specificity of G $\alpha$ q to that of G $\alpha$ i. *Nature* **363**, 274–276 (1993). [doi:10.1038/363274a0](https://doi.org/10.1038/363274a0) [Medline](#)

55. B. R. Conklin, P. Herzmark, S. Ishida, T. A. Voyno-Yasenetskaya, Y. Sun, Z. Farfel, H. R. Bourne, Carboxyl-terminal mutations of Gq alpha and Gs alpha that alter the fidelity of receptor activation. *Mol. Pharmacol.* **50**, 885–890 (1996). [Medline](#)
56. G. G. Gregorio, M. Masureel, D. Hilger, D. S. Terry, M. Juette, H. Zhao, Z. Zhou, J. M. Perez-Aguilar, M. Hauge, S. Mathiasen, J. A. Javitch, H. Weinstein, B. K. Kobilka, S. C. Blanchard, Single-molecule analysis of ligand efficacy in  $\beta_2$ AR-G-protein activation. *Nature* **547**, 68–73 (2017). [doi:10.1038/nature22354](https://doi.org/10.1038/nature22354) [Medline](#)
57. A. Peisley, G. Skiniotis, 2D Projection Analysis of GPCR Complexes by Negative Stain Electron Microscopy. *Methods Mol. Biol.* **1335**, 29–38 (2015). [doi:10.1007/978-1-4939-2914-6\\_3](https://doi.org/10.1007/978-1-4939-2914-6_3) [Medline](#)
58. D. N. Mastronarde, Automated electron microscope tomography using robust prediction of specimen movements. *J. Struct. Biol.* **152**, 36–51 (2005). [doi:10.1016/j.jsb.2005.07.007](https://doi.org/10.1016/j.jsb.2005.07.007) [Medline](#)
59. S. Q. Zheng, E. Palovcak, J.-P. Armache, K. A. Verba, Y. Cheng, D. A. Agard, MotionCor2: Anisotropic correction of beam-induced motion for improved cryo-electron microscopy. *Nat. Methods* **14**, 331–332 (2017). [doi:10.1038/nmeth.4193](https://doi.org/10.1038/nmeth.4193) [Medline](#)
60. K. Zhang, Gctf: Real-time CTF determination and correction. *J. Struct. Biol.* **193**, 1–12 (2016). [doi:10.1016/j.jsb.2015.11.003](https://doi.org/10.1016/j.jsb.2015.11.003) [Medline](#)
61. S. H. W. Scheres, RELION: Implementation of a Bayesian approach to cryo-EM structure determination. *J. Struct. Biol.* **180**, 519–530 (2012). [doi:10.1016/j.jsb.2012.09.006](https://doi.org/10.1016/j.jsb.2012.09.006) [Medline](#)
62. J. B. Heymann, Bsoft: Image and molecular processing in electron microscopy. *J. Struct. Biol.* **133**, 156–169 (2001). [doi:10.1006/jsbi.2001.4339](https://doi.org/10.1006/jsbi.2001.4339) [Medline](#)
63. A. Waterhouse, M. Bertoni, S. Bienert, G. Studer, G. Tauriello, R. Gumienny, F. T. Heer, T. A. P. de Beer, C. Rempfer, L. Bordoli, R. Lepore, T. Schwede, SWISS-MODEL: Homology modelling of protein structures and complexes. *Nucleic Acids Res.* **46** (W1), W296–W303 (2018). [doi:10.1093/nar/gky427](https://doi.org/10.1093/nar/gky427) [Medline](#)

64. E. F. Pettersen, T. D. Goddard, C. C. Huang, G. S. Couch, D. M. Greenblatt, E. C. Meng, T. E. Ferrin, UCSF Chimera—A visualization system for exploratory research and analysis. *J. Comput. Chem.* **25**, 1605–1612 (2004). [doi:10.1002/jcc.20084](https://doi.org/10.1002/jcc.20084) [Medline](#)
65. P. Emsley, B. Lohkamp, W. G. Scott, K. Cowtan, Features and development of Coot. *Acta Crystallogr. D Biol. Crystallogr.* **66**, 486–501 (2010). [doi:10.1107/S0907444910007493](https://doi.org/10.1107/S0907444910007493) [Medline](#)
66. P. D. Adams, P. V. Afonine, G. Bunkóczi, V. B. Chen, I. W. Davis, N. Echols, J. J. Headd, L.-W. Hung, G. J. Kapral, R. W. Grosse-Kunstleve, A. J. McCoy, N. W. Moriarty, R. Oeffner, R. J. Read, D. C. Richardson, J. S. Richardson, T. C. Terwilliger, P. H. Zwart, PHENIX: A comprehensive Python-based system for macromolecular structure solution. *Acta Crystallogr. D Biol. Crystallogr.* **66**, 213–221 (2010). [doi:10.1107/S0907444909052925](https://doi.org/10.1107/S0907444909052925) [Medline](#)
67. V. B. Chen, W. B. Arendall 3rd, J. J. Headd, D. A. Keedy, R. M. Immormino, G. J. Kapral, L. W. Murray, J. S. Richardson, D. C. Richardson, MolProbity: All-atom structure validation for macromolecular crystallography. *Acta Crystallogr. D Biol. Crystallogr.* **66**, 12–21 (2010). [doi:10.1107/S0907444909042073](https://doi.org/10.1107/S0907444909042073) [Medline](#)
68. T. D. Goddard, C. C. Huang, E. C. Meng, E. F. Pettersen, G. S. Couch, J. H. Morris, T. E. Ferrin, UCSF ChimeraX: Meeting modern challenges in visualization and analysis. *Protein Sci.* **27**, 14–25 (2018). [doi:10.1002/pro.3235](https://doi.org/10.1002/pro.3235) [Medline](#)
69. R. A. Friesner, R. B. Murphy, M. P. Repasky, L. L. Frye, J. R. Greenwood, T. A. Halgren, P. C. Sanschagrin, D. T. Mainz, Extra precision glide: Docking and scoring incorporating a model of hydrophobic enclosure for protein-ligand complexes. *J. Med. Chem.* **49**, 6177–6196 (2006). [doi:10.1021/jm051256o](https://doi.org/10.1021/jm051256o) [Medline](#)